Microstructural origins of cycle hardening behaviors and fracture mechanisms of 304L stainless steel during low-cycle fatigue

Wei Jiang [a], Shaojia Shi [c], Heng Wang [c], Kang Wei [d], Yonghao Zhao [b,c,*]

[a] School of Materials Science and Engineering, Anhui Polytechnic University, Wuhu 241000, China
[b] School of Materials Science and Engineering, Hohai University, Changzhou 213200, China
[c] Nano and Heterogeneous Materials Center, School of Materials Science and Engineering, Nanjing University of Science and Technology, Nanjing 210094, China
[d] School of Materials Science and Engineering, Nanchang Hangkong University, Nanchang 330063, China

ABSTRACT

Low-cycle fatigue behaviors of 304L stainless steel were investigated under different strain amplitudes (0.25 %, 0.3 %, 0.4 %, 0.5 %) and number of cycles to establish the relationship between macro-properties and micro-mechanisms. In all cases of strain amplitude, the 304L stainless steel displays a slight degree of cycle softening subsequent to the initial hardening in the cyclic stress–strain response. In the final stages of fatigue, the 304L stainless steel once again exhibits intense cycle hardening, contingent on the strain amplitude. In the two internal stress components of flow stress, the back stresses consistently exceed the effective stresses at varying strain amplitudes, demonstrating that the long-range resistance stresses for dislocation slip are larger than the short-range obstacles. Detailed microstructural investigation reveals that dislocations and stacking faults are the predominant microstructures observed at a low strain amplitude of 0.25 %. A phase transformation from FCC to HCP leads to cycle hardening at 0.3 % strain amplitude. At 0.4 % strain amplitude and above, the formation of dislocation substructures (veins, walls and cells) and BCC structural α' −martensite results in a more pronounced hardening effect, albeit at the cost of premature fracture. The present study offers a fundamental insight into the deformation mechanisms of 304L stainless steel during cyclic loading.

1. Introduction

The exceptional comprehensive properties of 304L austenitic stainless steel, including the superior strength-ductility combination, corrosion resistance and low-cost, have made it a material of choice for use as structural engineering applications [1–3]. The 304L austenitic stainless steel possesses low stacking fault energy (SFE), which gives rise to the prevalence of stacking fault (SF) and twinning as common deformation mechanisms during monotonic tensile deformation [4–7]. Moreover, phase transformation from face-centered cubic (FCC) austenite to either hexagonal close-packed (HCP) ε-martensite or α' −martensite with body-centered cubic (BCC) structure is also prevalent in 304L austenitic stainless steel, inducing dynamic Hall-Petch effect and high strain hardening ability [8]. The aforementioned mechanisms give rise to an excellent combination of strength and ductility in 304L austenitic stainless steels subjected to monotonic tensile deformation.

Fatigue performance of 304L austenitic stainless steel under repeated loading is another crucial evaluation condition, particularly in consideration of its potential application as a structural material. It is well established that the microstructural evolution under cyclic loading differs significantly from that under monotonic loading. For example, deformation twins and martensitic transformation are the primary factors responsible for high strain hardening in the Fe-22Mn-0.6C austenitic steel during monotonic loading, while only rearranged dislocation structures generate under cyclic loading without any twinning or phase transformation [9]. Consequently, the fatigue response of this steel in the low cycle fatigue (LCF) regime is featured by the presence of a stable stress plateau rather than cycle hardening, unless high density of twins are introduced by pre-deformation first [9].

The deformation mechanisms of FCC materials under cyclic loading are contingent upon a multitude of intrinsic and extrinsic factors, including SFE, strain amplitude, and the number of cycles. The pivotal function of the SFE can be succinctly encapsulated as follows: (i) persistent slip bands, wavy-substructures in materials with high SFE [10]; (ii) planar slip bands and SFs in materials with low to medium SFE [11]; (iii) mechanical twinning and phase transformation in materials

with lower SFE [12,13]. During cyclic deformation, a low SFE enables dislocation planar slip, contributing to enhanced reversible movement of dislocations and, consequently, superior fatigue properties [8]. For example, the fatigue mechanisms of CoCrNi medium-entropy alloy are featured by planar dislocation slip due to low SFE, contributing to longer lifetime at same strain amplitude than the CoCrFeMnNi high-entropy alloy [14,15]. Moreover, low SFE leads to the dissociation of perfect dislocations and generation of SFs. The activity of SFs can also be promoted to generate tetrahedral defects by applying nonproportional loading, which awakens more numbers of slip systems [16]. Twinning will result in dynamic grain refinement, thereby improving the strength of materials in question and relaxing the dislocation pile-up at grain boundaries [17]. Besides, the increased twin boundaries have the potential to alter grain orientations, impeding the propagation of fatigue cracks and consequently enhancing fatigue properties [17]. Nevertheless, deformation twin has been identified as potential crack propagation pathways in high-cycle fatigue [18]. With regard to phase transformation, the results are inconclusive as to their effect on fatigue behavior. The ε-martensite is usually generated by the overlapping of SFs on every second $\{111\}_\gamma$ planes, while the α'−martensite is formed by the direct transformation from γ-austenite directly, or the subsequent transformation $\gamma \rightarrow \varepsilon \rightarrow \alpha'$ [19,20]. In comparison to dislocation planar slip, the process of martensite transformation possesses is less reversible. The $\gamma \rightarrow \varepsilon$ transformation is reported that can help to arrest the crack growth [12], but has limited effect on cyclic hardening [21].While the α'-martensite transformation contributes to the strain hardening capacity [19]. The phase transformation may result in either crack arresting or crack coarsening, depending on the hardness and brittleness of the martensite produced rather than on the transformation process [22]. Despite the enhanced understanding of LCF response of austenitic stainless steel, there is a dearth of comprehensive information centering on the microstructural evolution at the submicron level and the interrelationship between microstructures and the cycle hardening behaviors and fracture mechanisms of 304L stainless steel, particularly under disparate cyclic straining conditions.

In current work, the LCF behavior and cycle hardening behavior of 304L stainless steel were investigated. The internal stress components of back stress and effective stress were analysed to reveal the dislocation slip behavior. The influence of strain amplitude on microstructural evolution during LCF deformation has been studied utilizing a range of characterization techniques, including scanning electron microscopy (SEM) coupled with electron backscatter diffraction (EBSD) and transmission electron microscopy (TEM) to establish the relationship between macro-properties and micro-mechanisms during LCF of 304L stainless steel.

2. Experiments

The 304L stainless steel was received with the chemical composition shown in Table 1. LCF specimens were prepared from the as-received sheets with a gauge length of 14 mm, a width of 4 mm and a thickness of 4 mm. The fatigue tests were performed on an Instron 8801 fatigue testing machine equipped with an extensometer of 10 mm in gauge length at room temperature. The strain-controlled mode was adopted with a strain ratio of R = -1 (ratio of minimum strain to maximum strain), a loading waveform of sinusoidal and a strain rate of 1×10^{-3} s^{-1}.The total strain amplitudes were 0.25 %, 0.30 %, 0.40 % and 0.50 %, respectively. Several tests are selected to be repeated twice or three times. Before fatigue tests, the specimens were electrolytic polished to obtain a strain-free and smooth surface.

Table 1
Chemical composition of the 304L stainless steel.

element	C	Si	Mn	P	S	Ni	Cr	Fe
wt%	0.02	0.36	1.23	0.026	0.005	8.1	18.21	Bal.

A Bruker-AXS D8 Advance X-ray diffractometer equipped with Cu-Kα radiation source is used for X-ray diffraction (XRD) analysis with 2θ of 30°-100°, scanning speed of 2°/min and step size of 0.005°. A Carl Zeiss-Auriga-45–66 SEM equipped with Oxford Instruments Aztec 2.0 EBSD system was used for EBSD acquisition under an operating voltage of 20 kV and a working distance of 12 mm. Binning of 4 × 4 and step size of 1 μm were adopted. Electrochemical polishing of the EBSD specimens were conducted in an electrolyte comprising 90 vol% acetic acid and 10 vol.% perchloric acid. The parameters were an applied voltage of 35 V and a polishing period of ~ 45 s. For TEM observations, an FEI-Tecnai G^2 20 S-TWIN microscope operating at 200 kV was employed. The TEM samples were extracted 2 mm away from the fracture surface of the post-fatigue specimens. Subsequently, the samples were subjected to mechanical grinding and electro-polishing in a twin jet electro-polishing system. The electrolyte contained 80 vol% acetic acid and 20 vol.% perchloric acid.

3. Results

3.1. Initial microstructure

As shown in Fig. 1a, the as-received 304L stainless steel exhibits a uniform equiaxed grain structure with an average grain size of ~ 43 μm. The inverse pole figure color code in Fig. 1a indicates a randomly distributed grain orientation devoid of any discernible texture. The XRD pattern in Fig. 1b reveals the single-phase FCC structure of the 304L stainless steel.

3.2. Cyclic response and fatigue lifetime

The cyclic responses of the 304L stainless steel at varying strain amplitudes are displayed in Fig. 2a, wherein the stress amplitudes are plotted against the number of cycles. As shown in Fig. 2a, the stress amplitude of 304L stainless steel exhibits an increase with strain amplitude, while the lifetime displays a monotonic decrease. The detailed lifetimes at different strain amplitudes are presented in Table 2. All curves exhibit a slight decrease (cyclic softening) in stress amplitude after the initial hardening stage (<10 cycles). For the sample tested at 0.25 % strain amplitude, a slight increase in stress amplitude is observed in the final stage prior to failure. At higher strain amplitudes of 0.3 % and above, there are indications of pronounced secondary hardening following the cyclic softening stage until failure, where the degree of secondary hardening depends on the strain amplitude. Hysteresis loops at several typical numbers of cycles of the samples fatigued at 0.3 %, 0.4 % and 0.5 % strain amplitudes are plotted to evaluate the degree of secondary hardening, as shown in Fig. 2b-d.

A comparison of the maximum stress amplitude with that at 1th cycle reveals an increase in stress amplitude at 0.3 % strain amplitude is approximately 64.9 MPa. This rises to 124.7 MPa and 307.6 MPa at 0.4 % and 0.5 % strain amplitudes, respectively. The hardening ratio (RH, $RH = (\sigma_a^{max} - \sigma_a^1)/\sigma_a^1$, where σ_a^1 and σ_a^{max} represent the stress amplitude at the first cycle and the maximum stress amplitude, respectively) can be employed to illustrate the extent of secondary cyclic hardening. Accordingly, the RH at stain amplitudes of 0.3 %, 0.4 % and 0.5 % are 0.27, 0.42 and 1.03, respectively.

The flow stress is comprised of two internal stress components, namely, back stress and effective stress. According to the Cottrell method [23–25], the decomposition of flow stress into back and effective stresses is conducted based on hysteresis loop analysis, as the schematic diagram presented in Fig. 3a. Fig. 3b-d exhibits the variations of back and effective stresses with the number of cycles at the strain amplitudes of 0.3 %, 0.4 % and 0.5 %, respectively. It is obvious that under all strain amplitudes, the back stresses are slightly greater than the effective stresses in the early stage, but much greater than the effective stresses in the late stage with the increase of the number of
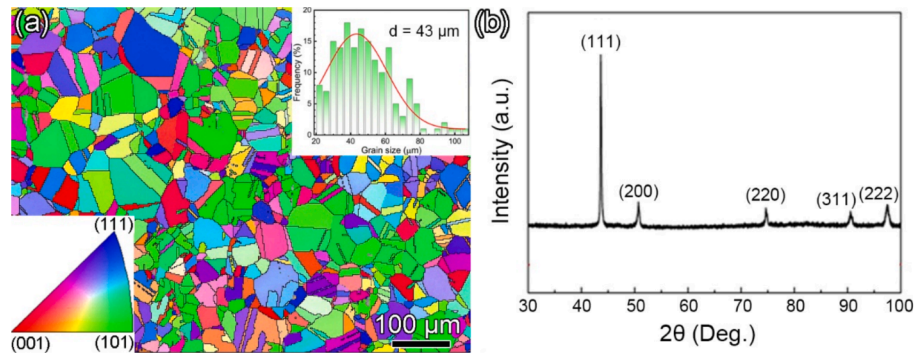
Fig. 1. (a) EBSD map of the 304L stainless steel prior to fatigue test. The inset in the upper right-hand corner displays the statistical grain size distribution. (b) The XRD pattern revealing the single-phase FCC structure of the 304L stainless steel.
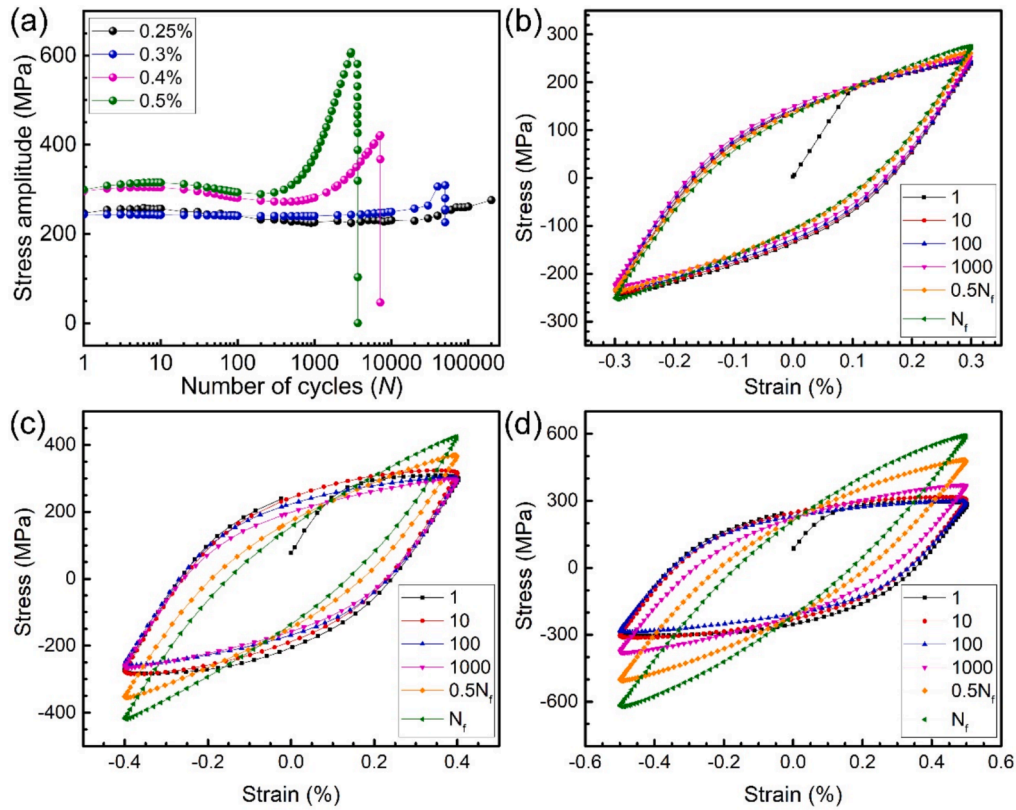

Fig. 2. (a) Stress amplitude vs. number of cycles curves for the 304L stainless steel under different strain amplitudes at room temperature. Hysteresis loops at several typical numbers of cycles for the samples fatigued at (b) 0.3 %, (c) 0.4 % and (d) 0.5 % strain amplitudes, respectively.

Table 2
The fatigue life of the 304L stainless steel at different strain amplitudes.

Strain amplitude (%)	0.25	0.3	0.4	0.5
Fatigue life (N)	175,175	49,577	7183	3658

cycles. The evolutions of back stresses nearly replicate the general trend of the stress amplitudes with three stages, e.g., initial hardening, a slight decrease in stress and a subsequent secondary hardening until failure. At 0.3 % strain amplitude, the effective stress remains nearly constant. While at 0.4 % and 0.5 % strain amplitudes, the effective stresses exhibit a marginal secondary hardening before failure. The degree of secondary hardening in effective stress at 0.5 % strain amplitude is larger than that at 0.4 % strain amplitude.

3.3. Microstructures after cyclic loading

The microstructural evolutions were investigated by post-mortem TEM analysis to reveal the deformation mechanisms of the 304L stainless steel during cyclic loading at different strain amplitudes. Fig. 4 depicts the bright-field (BF) TEM images of the samples tested at 0.25 % strain amplitude until failure. The inserted selected area electron diffraction (SAED) pattern was recorded at the [110] or [112] zone axis, but the BF TEM image was taken slightly off the zone axis in a two-beam condition to enhance the contrast of dislocations. As shown in Fig. 4a, dislocation planar slip is dominant mechanism, characterized by slip traces of edge-on (−111) slip plane. Additionally, planar slip bands (SBs) with dislocation arrangements (Fig. 4b) and SFs (Fig. 4c) are also observed, due to the planar slip of dislocations in 304L stainless steel with low SFE.

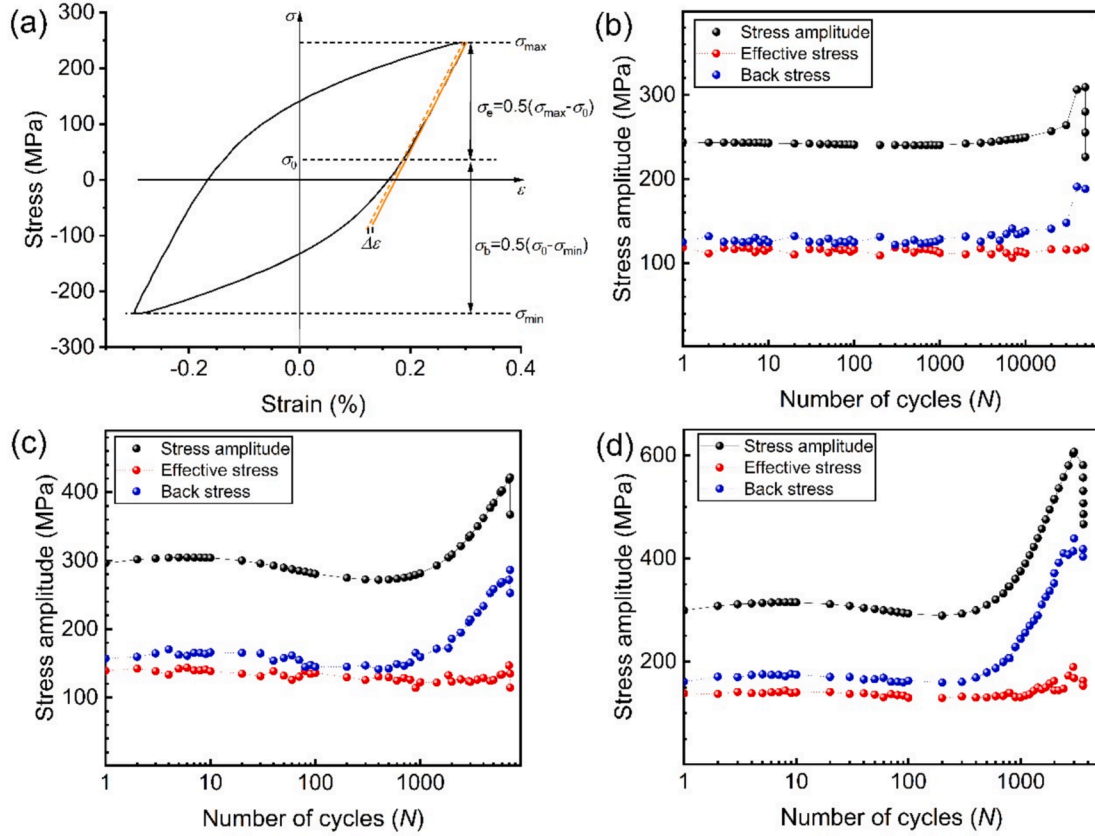Fig. 5 displays the BF TEM images of the samples tested at 0.3 %

Fig. 3. (a) Schematic diagram of stress decomposition to effective stress (σ_e) and back stress (σ_b) based on the Cottrell's method. Here, σ_0 is determined by first linearly fitting the elastic unloading regime of hysteresis loop, and then translating its parallel segment with a plastic strain offset ($\Delta\varepsilon$) of 0.01% to intersect with the hysteresis loop [26,27]. Variations of effective stress and back stress at the strain amplitudes of (b) 0.3%, (c) 0.4% and (d) 0.5%, respectively.

strain amplitude until failure. SFs still prevail, as shown in Fig. 5a. Besides, lamellar structures are observed (Fig. 5b). A detailed analysis of the SAED pattern in Fig. 5b reveals that the lamellar structures are deformation bands containing HCP structural ε phases, rather than deformation twins [13]. The orientation relationship between the ε phases and the FCC matrix is $(0001)_{HCP} \parallel (-111)_{FCC}$ and $[11-20]_{HCP} \parallel [01-1]_{FCC}$. Interrupted test was conducted at the 10000th cycle prior to the onset of the cyclic hardening stage and the corresponding microstructures were investigated to understand the effect of HCP phase transformation on the cyclic hardening behavior. As shown in Fig. 6, high dense dislocations featured by planar slip traces of edge-on (-111) slip plane, planar SB containing dislocation arrays and abundant SFs are main microstructures, accompanied by a small quantity of the HCP phase prior to the hardening stage. This suggests that the pronounced cycle hardening before fracture is related to the substantial formation of the HCP phase.

At a strain amplitude of 0.4 %, α' −martensite with BCC structure is observed in the presence of high dense dislocations and ε phases (Fig. 7a). As evidenced by the SAED pattern in the upper right corner of Fig. 7a, the three phases exhibit a consistent orientation relationship as $[111]_{BCC} \parallel [11-20]_{HCP} \parallel [01-1]_{FCC}$. Furthermore, at this strain amplitude, local dislocations rearrange into substructures, such as veins and walls. This is a consequence of the increased plastic deformation, leading to a transition from planar to wavy dislocation slip. Nevertheless, these structures are relatively ill-defined (e.g., the left and right sides of Fig. 7b), suggesting the domination of multiple-slip [28]. Further inspection along the crack by EBSD method reveals abundant α' −martensite around the crack, as shown in Fig. 8.

In comparison to the ill-defined dislocation substructures observed in samples tested at 0.4 % strain amplitude, the main substructures, including veins, walls and cells in the samples failure at 0.5 % strain

amplitude are well-developed (Fig. 9b-d). Mussy dislocations are observed between the dislocation walls (Fig. 9c), which are believed to be cross-slip dislocations with screw type [27–29]. Besides, the lamellar structures comprising HCP structural ε phases and BCC structural α' −martensite are still observed in Fig. 9a. The microstructures in the samples tested at 0.5 % strain amplitude after 10 cycles, corresponding to the initial point of the softening stage, are also observed to reveal the deformation mechanism. As shown in Fig. 10, planar dislocation slip and SFs are dominate deformation mechanisms, which are analogous to that observed in the samples failure at 0.25 % strain amplitude.

XRD experiments were performed to quantify the variation of phase transformation at different strain amplitudes. The quantitative estimation of phases by XRD data is based on the equation (1) [30,31]:

$$V_i = \frac{1/n \sum_{j=1}^{n} I_i^j / R_i^j}{1/n \sum_{j=1}^{n} \frac{I_\gamma^j}{R_\gamma^j} + 1/n \sum_{j=1}^{n} I_\varepsilon^j / R_\varepsilon^j + 1/n \sum_{j=1}^{n} I_{\alpha'}^j / R_{\alpha'}^j} \tag{1}$$

where i represents the γ, ε or α' phase, n is the number of examined peaks for particular phase, I is the integrated intensity of the diffraction peak, $R_{hkl} = \frac{1}{v^2} |F|^2 P(\frac{1+cos^2 2\theta}{cos\theta sin^2\theta}) e^{-2M}$ is the material scattering factor, v is the volume of the unit cell, F is the structure factor, P is multiplicity factor, e^{-2M} is temperature factor, θ is diffraction angle. As shown in Fig. 11a, the 304L stainless steel tested at 0.25 % strain amplitude until failure exhibits a single-phase FCC structure. After LCF deformation at 0.3 % strain amplitude, the (10–11) crystallographic plane for ε-martensite are observed, indicating the $\gamma \rightarrow \varepsilon$ transformation. Besides, minor peaks of the (110) and (211) crystallographic planes for α' −martensite are also detected at 0.3 % strain amplitude. With the strain amplitude increase, the volume fraction of ε-martensite remains almost unchanged, while the volume fraction of α' −martensite increases constantly (Fig. 11b).
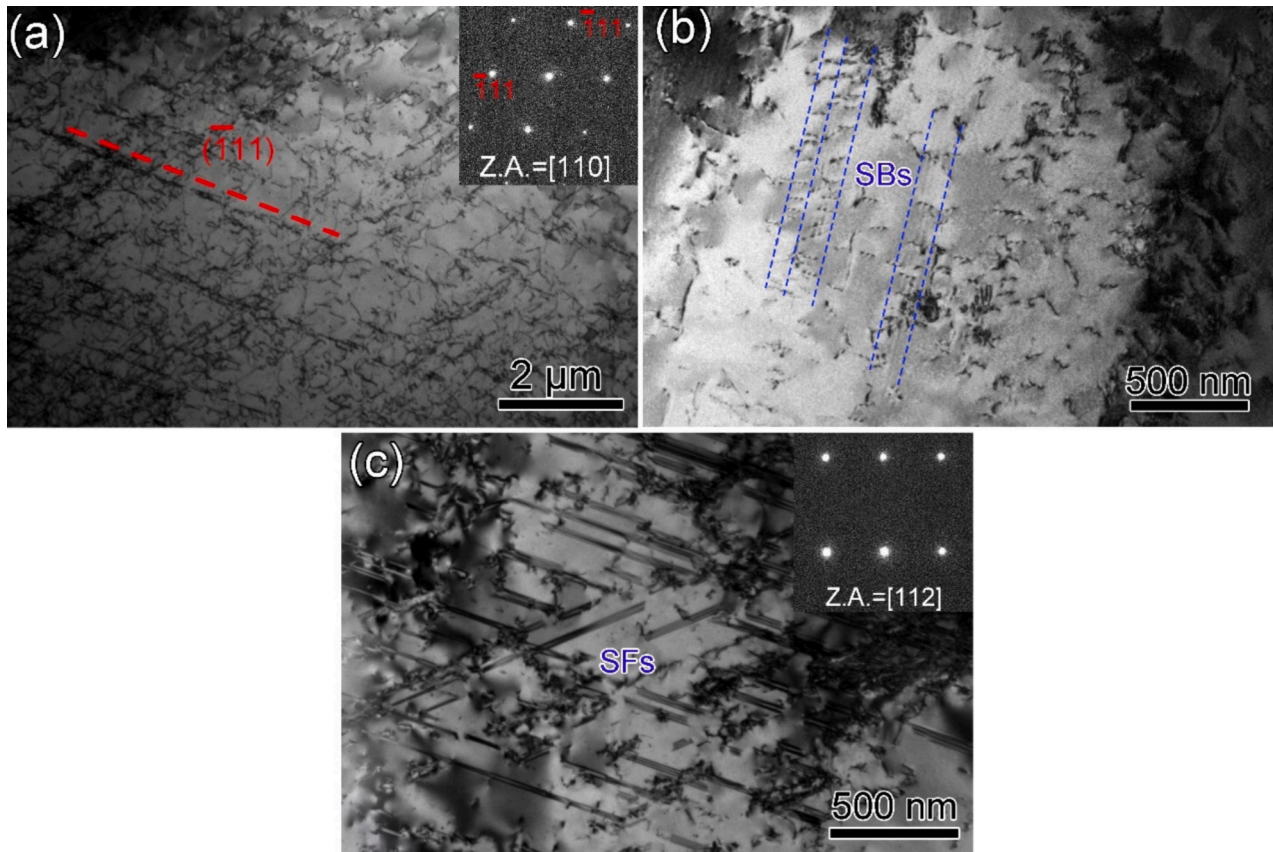
Fig. 4. Microstructures in the samples tested at 0.25% strain amplitude until failure. (a) Planar slip character verified by the trace of edge-on (−111) slip planes; (b) Planar slip bands (SBs); (c) Stacking faults (SFs).
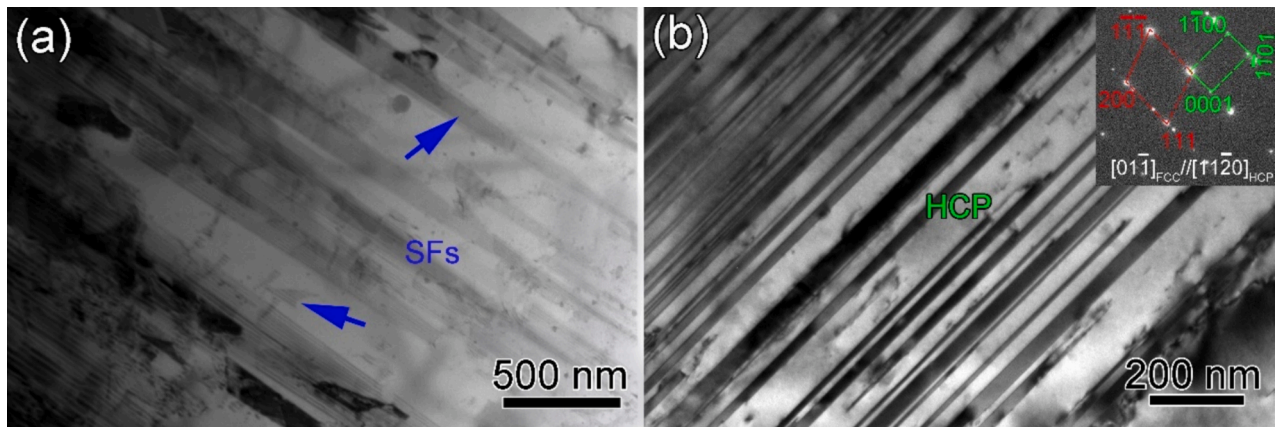

Fig. 5. Microstructures in the samples tested at 0.3% strain amplitude until failure. (a) SFs; (b) HCP structural ε-martensite lamellae.

This phenomenon is consistent with the TEM results that α' −martensite is combined with ε-martensite, which is continuously formed through the phase transformation sequence $\gamma \rightarrow \varepsilon \rightarrow \alpha'$ [19,20].

4. Discussions

4.1. Dependence of microstructural evolution on strain amplitude

The role of the applied strain amplitude in the microstructural evolution of materials subjected to cyclic loading is of paramount importance. As shown in Fig. 4, at a low strain amplitude of 0.25 % until failure, the activity of dislocation planar slip and SF is primarily observed, akin to that observed at low strain under monotonic loading.

The dislocation planar slip and SFs are attributed to the low SFE of the 304L stainless steel. The low SFE means comparatively large width of SFs, which in turn makes it more challenging to concentrate partial dislocations. Consequently, the frequency of cross slip is diminished and planar slip prevails [32]. Previous works have suggested that short-range ordering (SRO) structures in traditional concentrated FCC solid solutions [17,33] and medium-entropy alloys [34–36] are likely to result in a pronounced localization of dislocation motion on restricted {111} planes [17]. Nevertheless, the impact of the SRO structure is either inconsequential or negligible in the context of present 304L stainless steel, given its inherent characteristics of dilute solid solubility.

At the intermediate strain amplitudes (0.3 % and 0.4 %), the density of SFs increases greatly (Figs. 5 and 6). An increase in the strain
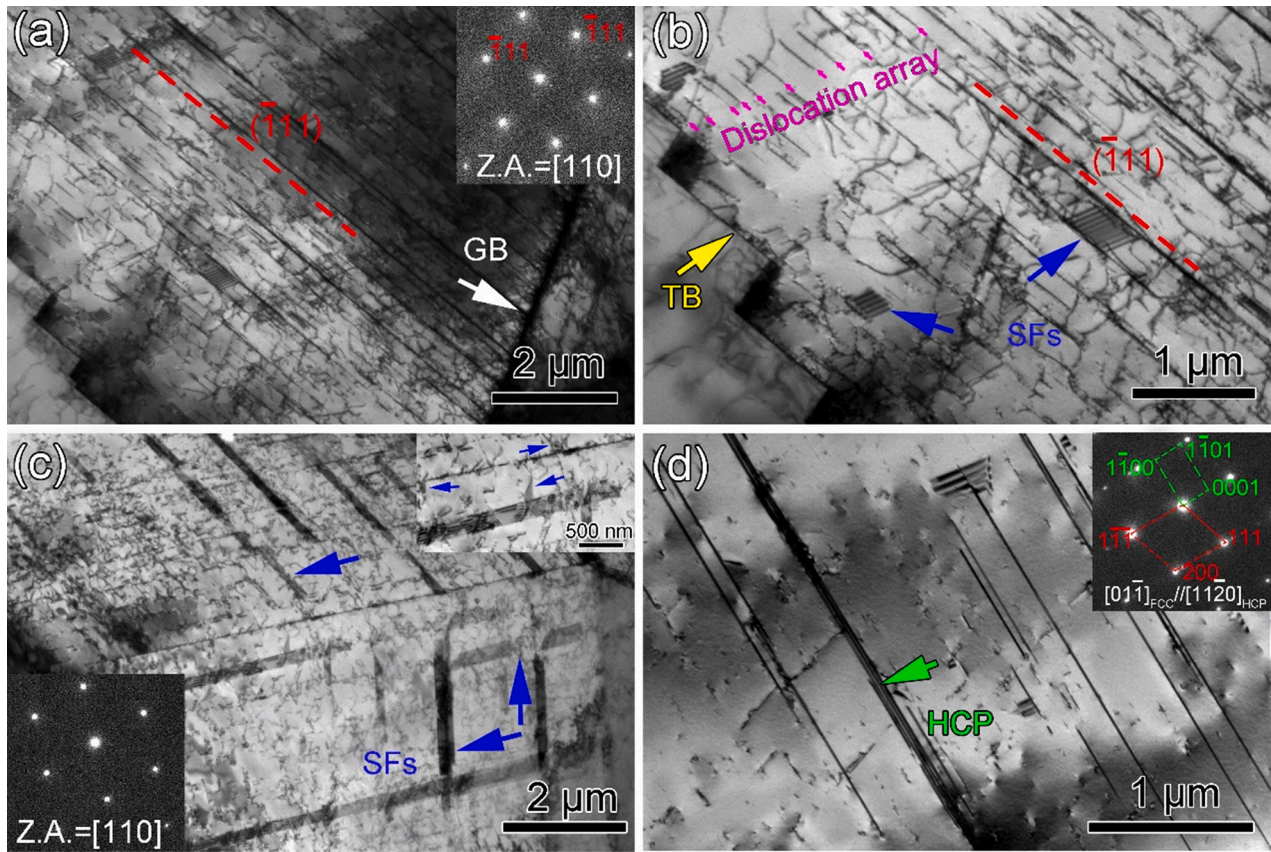
Fig. 6. Microstructures in the samples tested at 0.3% strain amplitude after 10,000 cycles, prior to the onset of cyclic hardening. (a-b) Dislocations, dislocation arrays within SB and SFs; (c) Stacking faults in different slip planes; (d) HCP structural ε-martensite lamellae.
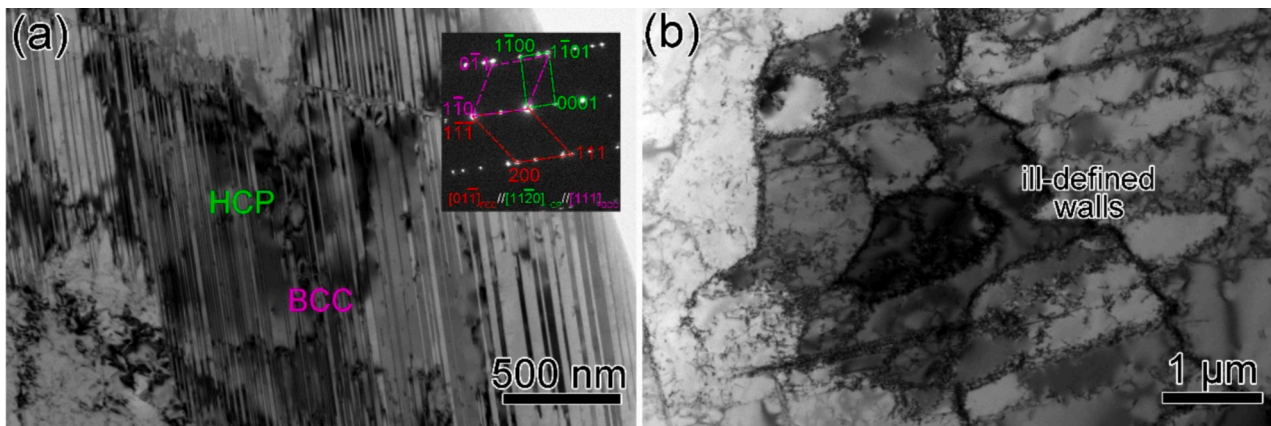

Fig. 7. Microstructures in the samples tested at 0.4% strain amplitude until failure. (a) HCP structural ε-martensite and BCC structural α' –martensite; (b) Ill-defined walls.

amplitude leads to a larger dissociation distance for partial dislocations and a wider SF, which is more difficult to recover under the action of reverse force. Considering the formation of SF by dissociating perfect dislocation into glissile leading and sessile trailing Shockley partials, the elevated density of SFs improves the probability of interaction between partial dislocation on two conjugated slip planes. Under the applied plastic strain, the occasional interaction between two glissile leading partials will form L-C lock containing a sessile stair-rod dislocation. While under irreversible plastic strain, the two trailing partials are capable of moving away from the formed sessile stair-rod dislocation, leading to the expansion of SF regions [37]. SFs usually are regarded as omens of deformation twining or strain-induced ε-martensite,

depending on the planar partial slip on every or every second slip plane, respectively. The predominant deformation mechanisms are closely related to the SFE like dislocation slip (>40mJ/m^2), slip and twining (20 ~ 40mJ/m^2) and martensitic transformation along with dislocation slip (<15 mJ/m^2) [37,38]. The SFE of present 304L stainless steel is 13.9 mJ/m^2 at room temperature [39], which is in the range typical for strain-induced HCP structural ε-martensite phase. In current work, no deformation twins are observed in all the examined samples. There may be a very small amount of deformation twins or very fine micro-twins locally that are missed. However, in any case, such a small amount of twins or tiny twins are not the main deformation mechanism under all strain amplitude conditions, and the influence on fatigue properties and
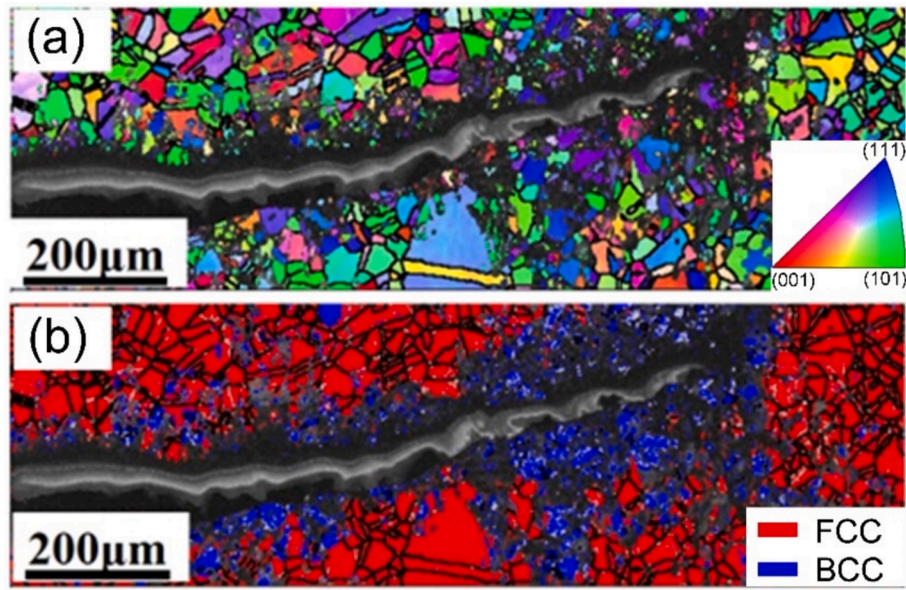
Fig. 8. EBSD images at the crack in the samples tested at 0.4% strain amplitude until failure. (a) IPF image; (b) Phase image.
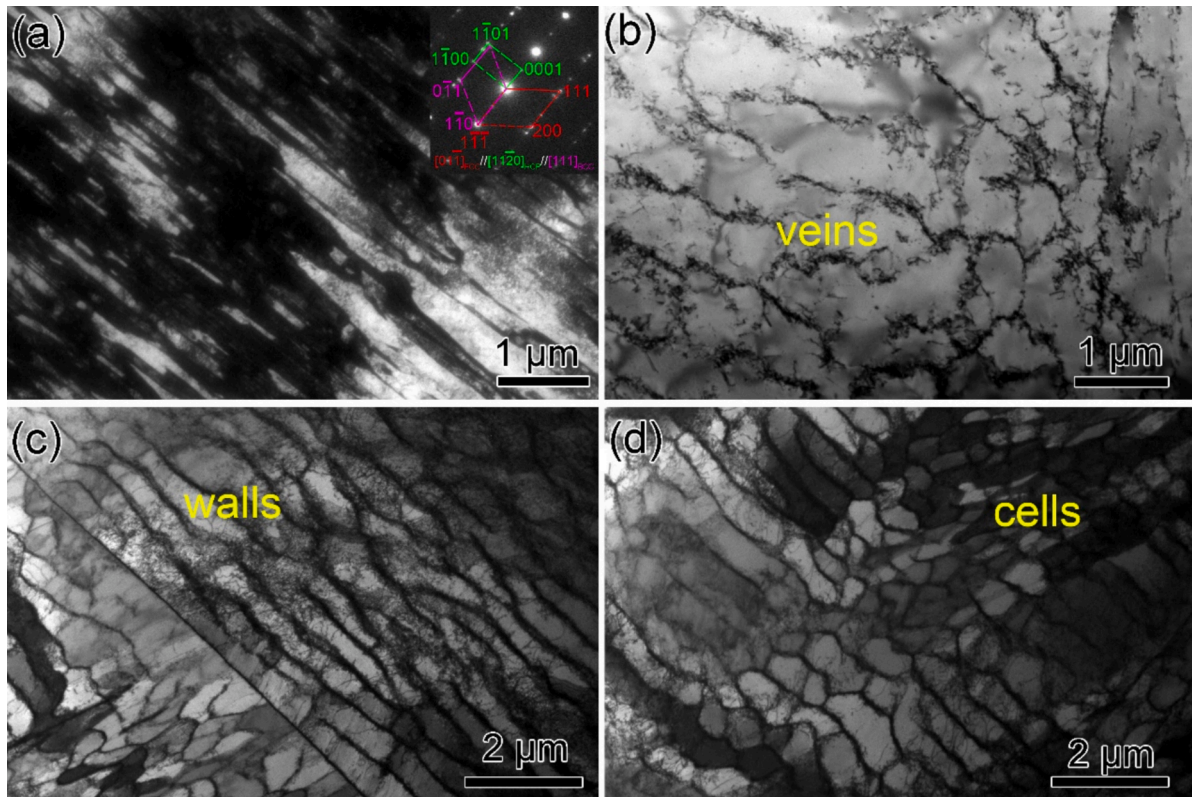

Fig. 9. Microstructures in the samples tested at 0.5% strain amplitude until failure. (a) HCP structural ε-martensite laminates and BCC structural α' −martensite; (b) Veins; (c) Walls; (d) Cells.

hardening behavior is minimal [28]. At 0.3 % strain amplitude and above, the SFs act as nucleation sites, facilitating the phase transformation from FCC to HCP through the mechanism of overlapping of faults on every second slip plane (Fig. 5b, 6d, 7a and 11). The α' −martensite is formed within the deformation bands via the intermediate ε-martensite, and the volume fraction increases with strain amplitude (Fig. 7a and 11), similar to that observed in other austenitic steels [40,41]. Especially, high dense α' −martensite forms around the

crack as a result of strain concentration (Fig. 8).

At the high strain amplitude of 0.5 %, dislocation-rich regions, including veins, walls and cells, are generated with scattered dislocations distributed in the channel (Fig. 9). The formation of such dislocation-rich structures is attributed to elevated dislocation density and changed dislocation slip model [26,27]. The multiplication of dislocations and the slip model of 304L stainless steel changed from planar-slip to wavy-slip contributes to the interaction and rearrangement of
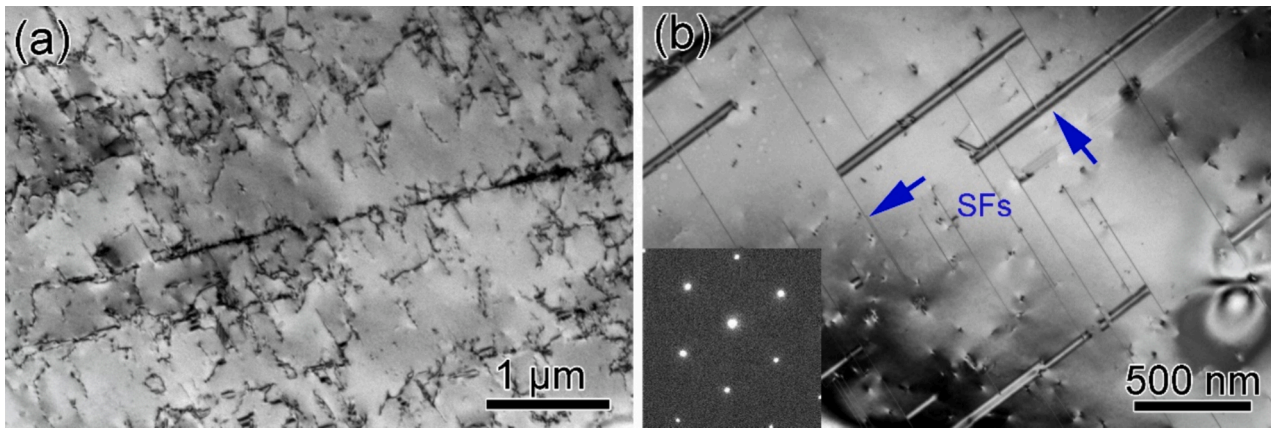
Fig. 10. Microstructures in the samples tested at 0.5% strain amplitude after 10 cycles, representing the initial point of the cyclic softening. (a) Scattered dislocation; (b) SFs on two slip planes.
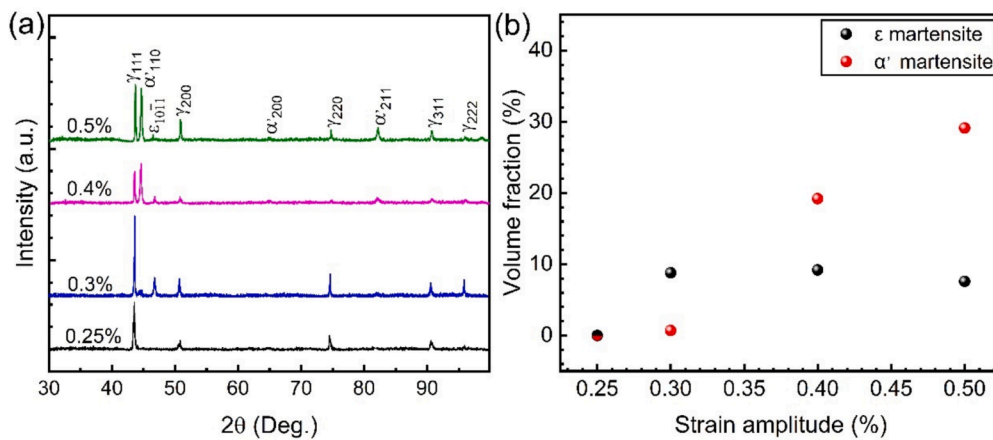

Fig. 11. (a) XRD patterns of the 304L stainless steel after tested at different strain amplitudes until failure. (b) Evolutions of the volume fraction of ε- and α' −martensite with strain amplitude.

dislocations. As reported in previous work, the formation of ill-defined veins is attributed to either a wavy-slip mode featured by extensive cross-slip or the activation of a multiple-slip system [28]. Subsequently, the metastable veins will evolute to dislocation walls [42–44] and finally to dislocation cell structures upon further loading [42,45]. Indeed, at the higher strain amplitude of 0.5 %, the formation of cell structures is observed to occur with greater frequency than that in samples tested at 0.4 % strain amplitude. In conclusion, the results suggest that an increase in strain amplitude leads to a transition of slip mode from planar-slip to wavy-slip (i.e., veins, walls, and cells) in the 304L stainless steel.

4.2. Microscopic analysis of hardening behavior and fatigue lifetime

During LCF deformation, the low hardening ability is indicative of a strain relaxation due to deformation reversibility, while strong hardening demonstrates the multiplication of dislocations and followed by substructure formation [12,46]. Obviously, the fatigue behaviors of 304L stainless steel, including fatigue lifetime, fatigue cracking and cyclic hardening/softening, are intimately connected to the microstructural evolution. As shown in Figs. 4-10, dislocation slip model, SFs and phase transformation are key factors influencing the fatigue lifetime and the equilibrium between cyclic hardening and softening. Accordingly, the following discussion will concentrate on the effects of slip mode, SFs and phase transformation.

4.2.1. Influence of slip model and SFs

In general, the dislocation slip mode is affected greatly by the SFE [32], SRO [33] and loading condition [47]. For present 304L stainless steel, the intrinsic condition of SFE and the loading condition with regard to strain amplitude are the principal factors that exert influence on the slip modes.

At a low strain amplitude of 0.25 %, the 304L stainless steel deforms by dislocation planar slip and SFs (Fig. 4). As previously stated, either a low SFE or SRO could result in planar slip [35]. In comparison, planar slip resulting from the low SFE of 304L stainless steel possesses better deformation homogeneity and reversibility than that initiated by the disordering of SROs. In the latter case, local strain concentration caused by dislocation pile-up in the slip band leads to poor deformation uniformity and damage accumulation [17]. At 0.25 % strain amplitude, the enhanced slip planarity means both decreased dislocation recovery rate due to suppressed cross-slip and reduced interactions from the cross-slip plane. Moreover, a considerable number of SFs are identified (Fig. 4), indicating the suppression of cross slip and enhanced deformation homogeneity. Thus, the 304L stainless steel exhibits the longest lifetime at low strain amplitude of 0.25 % but low hardening rate due to improved deformation reversibility (Fig. 2). At 0.3 % strain amplitudes, the density of SF increases notably (Figs. 5 and 6). SFs are reported that could act as obstacles to hinder dislocation motion, where the interaction between dislocations and SFs will lead to strain hardening [48–50]. Therefore, the secondary hardening in 304L stainless steel tested at 0.3 % strain amplitudes and above, is partly due to the increase of SF

density.

At high strain amplitudes of 0.4 % and 0.5 %, the dislocation cross slip to another slip system is easy. As shown in Figs. 7 and 9, dislocation wavy slip and dislocation interactions are promoted due to increased degree of accumulated plastic deformation at 0.4 % and 0.5 % strain amplitudes. This leads to the rearrangement of dislocations into sub-structures comprising veins, cells and walls. The cross slip can relax the strain concentration and reduce dislocation density, leading to cyclic softening. However, the formation of substantial dislocation walls and cells provides obstacles for dislocation slip and decreases the mean free path of dislocation slip, contributing to the secondary hardening of 304L stainless steel.

4.2.2. Influence of phase transformation

In a fully symmetric push–pull LCF loading, cyclic plastic deformation is mediated by several simultaneously activated deformation mechanisms, of which interactions between these mechanisms result in strain hardening. In particular, the martensite is renowned for its pronounced interaction with the other crystal defects. In previous work, the author reported that the homogeneity and morphology of ε-martensitic and other planar slip deformation products may correlate more directly with the hardening than α'−martensite for 304 stainless steel under nonproportional straining condition [16]. While in present work, the deformation induced ε-martensitic transformation firstly occurred at 0.3 % strain amplitude, accompanied by a significant prevalence of dislocation planar slip and SFs (Figs. 5 and 6). During symmetric cyclic loading, the formed ε-martensitic/matrix interfaces act as strong obstacles to dislocation slip, inducing obvious cycle hardening (Fig. 2a). In comparison to ε-martensite, the α'−martensite mass-generated at 0.4 % strain amplitude (Figs. 7 and 11) exerts a more pronounced influence on the cycle hardening, as illustrated in Fig. 2a. This phenomenon has also been documented by Glage et al., who have demonstrated that α'−martensite formed from austenite is responsible for a high degree of cyclic hardening at higher strain amplitudes [13]. Large amounts of interfaces introduced by ε- and α'−martensite phase transformation create additional obstacles, reducing the mean free path of dislocation motion. Therefore, a conclusion can be drawn that the formation of substantial dislocation walls and cells (mentioned above) and higher dense phase interfaces induced by α'−martensite (Fig. 11b) are responsible for the steeper hardening at the highest strain amplitude of 0.5 %.

Martensite transformation is also reported that have a dual role in influencing fatigue lifetime, e.g., transformation-mediated crack arresting preventing crack growth and transformation-mediated crack coalescence promoting crack growth [22]. According to the results in present work, the effects of ε-martensite and α'−martensite on the fatigue lifetime are quite different. As shown in Fig. 2a, the emergence of α'−martensite leads to a dramatic decline in fatigue lifetime, from 49577 *N* at 0.3 % strain amplitude to 7183 *N* at 0.4 % strain amplitude. Previous work has established that strain is predominantly accommodated by the FCC phase, whereas stress is primarily accommodated by the HCP phase [37]. Bidirectional transformation is feasible between FCC and HCP phases, allowing for the accommodation of cyclic plastic deformation and the introduction of transformation-induced toughening, which is conducive to damage resistance and fatigue performance at 0.3 % strain amplitude [37]. Moreover, the generated HCP martensite maintains the Shoji-Nishiyama orientation relationship with the γ-austenite matrix, as shown in the SAED pattern in Fig. 5b. The coherent phase boundaries of the two phases lead to optimal strain and stress distributions, which in turn reduce the potential for damage nucleation [51]. At strain amplitudes in excess of 0.4 %, the formation of α'-martensite is detrimental to the fatigue life. The formed α'-martensite will act as the preferential sites of crack initiation. Furthermore, cracking along the FCC-BCC phase interfaces may accelerate crack propagation (Fig. 8), prejudicing the lifetime.

4.2.3. Evolutions of internal stress components

The evolution of internal back and effective stresses in Fig. 3 provides insight into the nature of dislocation activities. For dislocation motion, the effective stress can help the dislocation overcome the short-range obstacles induced by lattice friction, solutes, dislocation forest and nano-precipitates [23,52–54]. As shown in Fig. 3b, the effective stress is independent of the number of cycles at 0.3 % strain amplitude, indicating that lattice friction and solution strengthening are main short-range obstacles for dislocation motion. At 0.3 % strain amplitude, planar dislocation activity is dominant, characterized by the SBs and SFs (Fig. 6), apart from HCP transformation at the final stage (Fig. 5). The planar dislocation activity contributes little to the effective stress due to the lack of dislocation forest strengthening caused from dislocations in other slip systems. At 0.4 % and 0.5 % strain amplitudes, the planar dislocation activity still prevails at the early stage (Fig. 10), leading to stable effective stresses. While at the final stage, dislocation cross-slip and multiple-slip are activated, promoting the formation of dislocation forest and leading to the secondary hardening in effective stresses (Fig. 3c and d).

In contrast, back stress is long-range resistance stress caused by strain incompatibilities, grain boundaries and dislocation substructures (dislocation walls and cells) [25]. At all strain amplitudes, the back stresses nearly replicate the general trend of the stress amplitudes, responsible for the hardening and softening in stress amplitudes (Fig. 3b-d). At the early stage, the marginal increase in back stress is mainly attributed to the accumulation of dislocations at grain boundaries and formed L-C locks [26]. Subsequently, softening happens due to the fact that the rate of dislocation generation is less than that of dislocation annihilation [55]. The reasons for secondary hardening in back stresses vary with strain amplitudes. At 0.3 % strain amplitude, a modest increase in back stress is observed at the final stage, indicating that the ε-martensitic/matrix interfaces and strain incompatibilities between two phases exert dominant effects on the long-range resistance stress for dislocation movement. At higher strain amplitudes of 0.4 % and 0.5 %, more pronounced enhancements in back stresses are observed at the final stage. These phenomena are attributed to the formation of dislocation substructures (walls and cells) (Figs. 7 and 9) and martensite transformation (Fig. 11b). The process of dislocation rearrangement into substructures (walls and cells) is linked to back stress softening [26]. However, the generated dislocation walls and cells provide obstacles for dislocation motion and reduce the mean free path of dislocation slip. Thus, the increased dislocation density contributes to the secondary hardening in back stresses. Moreover, dynamic formation of ε- and α'-martensite introduces high dense phase interfaces and improved strain incompatibilities, contributing to the elevated back stresses. Higher volume fraction of α'−martensite (Fig. 11b) leads to a steeper increase in back stress at the highest strain amplitude of 0.5 %. To sum up, the consistently greater back stresses than the effective stresses at different strain amplitudes (Fig. 3) indicate that the long-range resistance stresses for dislocation slip are larger than the short-range obstacles [25,54].

5. Conclusions

The fatigue behaviors and corresponding deformation mechanisms of 304L stainless steels were comprehensively investigated at different strain amplitudes. The main conclusions are as follows:

1. The 304L stainless steel exhibits a superior fatigue property at 0.25 % strain amplitude. The increase of stain amplitude leads to higher degrees of secondary hardening, but reductions in lifetime.
2. As the strain amplitude rise, the predominant deformation mechanisms change from dislocation planar slip and the formation of SFs to FCC → HCP phase transformation, and finally to the formation of dislocation substructures (veins, walls and cells) and BCC structural α'−martensite.

3. The back stresses are always greater than the effective stresses, demonstrating that the long-range resistance stresses for dislocation slip are larger than the short-range obstacles. Lattice friction and solution strengthening contribute to a stable effective stress, while dislocation cross-slip and multiple-slip promote the formation of dislocation forest and lead to the secondary hardening in effective stress. The increased dislocation density, dynamic introduction of high dense phase interfaces and improved strain incompatibilities by forming α'-martensite and ε-martensitic, jointly contribute to the secondary hardening in back stress.

CRediT authorship contribution statement

Wei Jiang: Writing – original draft, Visualization, Funding acquisition, Data curation. **Shaojia Shi:** Data curation, Investigation. **Heng Wang:** Investigation. **Kang Wei:** Funding acquisition. **Yonghao Zhao:** Writing – review & editing, Supervision, Funding acquisition, Conceptualization.

Declaration of competing interest

The authors declare that they have no known competing financial interests or personal relationships that could have appeared to influence the work reported in this paper.

Acknowledgements

Data availability

Data will be made available on request.

References

[1] Zhang HW, Zhao YM, Wang YH, Yu HX, Zhang CL. Fabrication of nanostructure in inner-surface of AISI 304 stainless steel pipe with surface plastic deformation. J Mater Res Technol 2018;34:2125–30.

[2] Kosaki A. Evaluation method of corrosion lifetime of conventional stainless steel canister under oceanic air environment. Nucl Eng Des 2008;238:1233–40.

[3] Jiang W, Cao Y, Jiang YD, Liu YF, Mao QZ, Zhou H, et al. Effects of nanostructural hierarchy on the hardness and thermal stability of an austenitic stainless steel. J Mater Res Technol 2021;12:376–84.

[4] Jiang W, Zhu KR, Li JS, Qin WB, Zhou J, Li ZM, et al. Extraordinary strength and ductility of cold-rolled 304L stainless steel at cryogenic temperature. J Mater Res Technol 2023;26:2001–8.

[5] Liu T, Li JS, Cheng W, Li ZM, Jiang W, Qin WB, et al. Formation mechanisms of heterostructures in 304L stainless steel processed by cold rolling and annealing. Vacuum 2024;223:113104.

[6] Liu J, Kaoumi D. Use of in-situ TEM to characterize the deformation-induced martensitic transformation in 304 stainless steel at cryogenic temperature. Mater Charact 2018;136:331–6.

[7] Steinmetz DR, Jäpel T, Wietbrock B, Eisenlohr P, Gutierrez-Urrutia I, Saeed-Akbari A, et al. Revealing the strain-hardening behavior of twinning-induced plasticity steels: Theory, simulations, experiments. Acta Mater 2013;61:494–510.

[8] Nikulin I, Sawaguchi T, Ogawa K, Tsuzaki K. Effect of γ to ε martensitic transformation on low-cycle fatigue behaviour and fatigue microstructure of Fe–15Mn–10Cr–8Ni–xSi austenitic alloys. Acta Mater 2016;105:207–18.

[9] Niendorf T, Lotze C, Canadinc D, Frehn A, Maier HJ. The role of monotonic pre-deformation on the fatigue performance of a high-manganese austenitic TWIP steel. Mater Sci EngA 2009;499:518–24.

[10] Li P, Li SX, Wang ZG, Zhang ZF. Fundamental factors on formation mechanism of dislocation arrangements in cyclically deformed fcc single crystals. Prog Mater Sci 2011;56:328–77.

[11] Suresh S. Fatigue of Materials. Cambridge University Press; 1998.

[12] Nikulin I, Sawaguchi T, Tsuzaki K. Effect of alloying composition on low-cycle fatigue properties and microstructure of Fe–30Mn–(6−x)Si–xAl TRIP/TWIP alloys. Mater Sci EngA 2013;587:192–200.

[13] Glage A, Weidner A, Biermann H. Effect of austenite stability on the low cycle fatigue behavior and microstructure of high alloyed metastable austenitic cast TRIP steels. Procedia Eng 2010;2:2085–94.

[14] Lu KJ, Chauhan A, Walter M, Tirunilai AS, Schneider M, Laplanche G, et al. Superior low-cycle fatigue properties of CoCrNi compared to CoCrFeMnNi. Scr Mater 2021;194:113667.

[15] Lu KJ, Chauhan A, Litvinov D, Schneider M, Laplanche G, Aktaa J. Cooperative deformation mechanisms in a fatigued CoCrNi multi-principal element alloy: A case of low stacking fault energy. J Mech Phys Solids 2023;180:105419.

[16] McDowell DL, Stahl OK, Stock SR, Antolovich SD. Biaxial path dependence of deformation substructure of type 304 stainless steel. Metall Trans 1988;19:1277–93.

[17] Shao CW, Zhang P, Liu R, Zhang ZJ, Pang JC, Duan QQ, et al. A remarkable improvement of low-cycle fatigue resistance of high-Mn austenitic TWIP alloys with similar tensile properties: Importance of slip mode. Acta Mater 2016;118:196–212.

[18] Kim YK, Ham GS, Kim HS, Lee KA. High-cycle fatigue and tensile deformation behaviors of coarse-grained equiatomic CoCrFeMnNi high entropy alloy and unexpected hardening behavior during cyclic loading. Intermetallics 2019;111:106486.

[19] Das A, Sivaprasad S, Chakraborti PC, Tarafder S. Morphologies and characteristics of deformation induced martensite during low cycle fatigue behaviour of austenitic stainless steel. Mater Sci EngA 2011;528:7909–14.

[20] Farias F, Alvarez-Armas I, Armas AF. On the strain-induced martensitic transformation process of the commercial AISI 304 stainless steel during cyclic loading. Int J Fatigue 2020;140:105809.

[21] Niendorf T, Thomas Wegener ZM, Li DR. Unexpected cyclic stress-strain response of dual-phase high-entropy alloys induced by partial reversibility of deformation. Scr Mater 2018;143:2018.

[22] Wang XG, Liu CH, Sun BH, Ponge D, Jiang C, Raabe D. The dual role of martensitic transformation in fatigue crack growth. Proc Natl Acad Sci 2022;119.

[23] Cottrell AH, Dexter DL. Dislocations and plastic flow in crystals. Am J Phys 1954;22:242–3.

[24] Kuhlmann-Wilsdorf D, Laird C. Dislocation behavior in fatigue II. Friction stress and back stress as inferred from an analysis of hysteresis loops. Mater Sci Eng 1979;37:111–20.

[25] Lu KJ, Chauhan A, Knöpfle F, Aktaa J. Effective and back stresses evolution upon cycling a high-entropy alloy. Mater Res Lett 2022;10:369–76.

[26] Sisodia S, Rajkowski M, Laplanche G, Chauhan A. Cyclic deformation behavior of an equiatomic CrFeNi multi-principal element alloy. Int J Fatigue 2023;174:107723.

[27] Sisodia S, Laplanche G, Rajkowski M, Chauhan A. Enhancing fatigue resistance of Cr-Mn-Fe-Co-Ni multi-principal element alloys by varying stacking fault energy and sigma (σ)-phase assisted grain-size reduction. Int J Fatigue 2025;191:108704.

[28] Lu KJ, Chauhan A, Tirunilai AS, Freudenberger J, Kauffmann A, Heilmaier M, et al. Deformation mechanisms of CoCrFeMnNi high-entropy alloy under low-cycle-fatigue loading. Acta Mater 2021;215:117089.

[29] Laird C, Charsley P, Mughrabi H. Low energy dislocation structures produced by cyclic deformation. Mater Sci Eng 1986;81:433–50.

[30] De AK, Murdock DC, Mataya MC, Speer JG, Matlock DK. Quantitative measurement of deformation-induced martensite in 304 stainless steel by X-ray diffraction. Scr Mater 2004;50:1445–9.

[31] Moser NH, Gross TS, Korkolis YP. Martensite formation in conventional and isothermal tension of 304 austenitic stainless steel measured by X-ray diffraction. Metall Mater Trans A 2014;45:4891–6.

[32] Sun Ig H, Laird C. Cyclic deformation behaviour of Cu-16at.%Al single crystals part II: Cyclic hardening and slip band behavior. Mater Sci EngA 1990;128:55–75.

[33] Gerold V, Karnthaler HP. On the origin of planar slip in f.c.c. alloys. Acta Metall 1989;37:2177–83.

[34] Li QJ, Sheng H, Ma E. Strengthening in multi-principal element alloys with local-chemical-order roughened dislocation pathways. Nat Commun 2019;10:3563.

[35] Jiang W, Yuan SY, Cao Y, Zhang Y, Zhao YH. Mechanical properties and deformation mechanisms of a $Ni_2Co_1Fe_1V_{0.5}Mo_{0.2}$ medium-entropy alloy at elevated temperatures. Acta Mater 2021;213:116982.

[36] Jiang W, Cao Y, Yuan SY, Zhang Y, Zhao YH. Creep properties and deformation mechanisms of a $Ni_2Co_1Fe_1V_{0.5}Mo_{0.2}$ medium-entropy alloy. Acta Mater 2023;245:118590.

[37] Bahadur F, Jain R, Biswas K, Gurao NP. Low cycle fatigue behaviour of non-equiatomic TRIP dual-phase $Fe_{50}Mn_{30}Co_{10}Cr_{10}$ high entropy alloy. Int J Fatigue 2022;155:106545.

[38] Wong SL, Madivala M, Prahl U, Roters F, Raabe D. A crystal plasticity model for twinning- and transformation-induced plasticity. Acta Mater 2016;118:140–51.

[39] Li JS, Cheng W, Qin WB, Chen M, Zhao Y, Li YS, et al. Cryogenic impact property of a high-strength-ductility 304L stainless steel with heterogeneous lamella structure. J Mater Res Technol 2023;24:1401–9.

[40] Venables JA. The martensite transformation in stainless steel. Philos Mag 1962;7: 35–44.

[41] Kelly PM. The martensite transformation in steels with low stacking fault energy. Acta Metall 1965;13:635–46.

[42] Mughrabi H. Dislocation wall and cell structures and long-range internal stresses in deformed metal crystals. Acta Metall 1983;31:1367–79.

[43] Gerland M, Mendez J, Violan P, Saadi BA. Evolution of dislocation structures and cyclic behaviour of a 316L-type austenitic stainless steel cycled in vacuo at room temperature. Mater Sci EngA 1989;118:83–95.

[44] Basinski SJ, Basinski ZS, Howie A. Early stages of fatigue in copper single crystals. Philos Mag 1969;19:899–924.

[45] Gerland M, Violan P. Secondary cyclic hardening and dislocation structures in type 316 stainless steel at 600 °C. Mater Sci Eng 1986;84:23–33.

[46] Sangid MD, Pataky GJ, Sehitoglu H, Rateick RG, Niendorf T, Maier HJ. Superior fatigue crack growth resistance, irreversibility, and fatigue crack growth–microstructure relationship of nanocrystalline alloys. Acta Mater 2011;59: 7340–55.

[47] Li XW, Peng N, Wu XM, Wang ZG. Plastic-strain-amplitude dependence of dislocation structures in cyclically deformed ⟨112⟩-oriented Cu-7 at. pct Al alloy single crystals. Metall Mater Trans A 2014;45:3835–43.

[48] Mecking H, Kocks UF. Kinetics of flow and strain-hardening. Acta Metall 1981;29 (11):1865–75.

[49] Kocks UF, Mecking H. Physics and phenomenology of strain hardening: the FCC case. Prog Mater Sci 2003;48:171–273.

[50] Jiang W, Gao XZ, Guo YZ, Chen X, Zhao YH. Dynamic impact behavior and deformation mechanisms of $Cr_{26}Mn_{20}Fe_{20}Co_{20}Ni_{14}$ high-entropy alloy. Mater Sci EngA 2021;824:141858.

[51] Jiang W, Gao XZ, Cao Y, Liu YF, Mao QZ, Gu L, et al. Charpy impact behavior and deformation mechanisms of $Cr_{26}Mn_{20}Fe_{20}Co_{20}Ni_{14}$ high-entropy alloy at ambient and cryogenic temperatures. Mater Sci EngA 2022;837:142735.

[52] Bouaziz O, Moon J, Kim HS, Estrin Y. Isotropic and kinematic hardening of a high entropy alloy. Scr Mater 2021;191:107–10.

[53] Mughrabi H. Deformation-induced long-range internal stresses and lattice plane misorientations and the role of geometrically necessary dislocations. Philos Mag 2006;86:4037–54.

[54] Feaugas X. On the origin of the tensile flow stress in the stainless steel AISI 316L at 300 K: back stress and effective stress. Acta Mater 1999;47:3617–32.

[55] Yang JY, Li BB, Wang K, Zhao L, Xu LY, Chen X. Cyclic deformation behavior and damage mechanism of 316H stainless steel under low-cycle fatigue loading at 650 °C. Int J Fatigue 2024;188:108523.